

Conductance-dependent Photoresponse in a Dynamic SrTiO₃ Memristor for Biorealistic Computing

Christoph Weilenmann¹, Hanglin He¹, Marko Mladenović¹, Till Zellweger¹, Kevin Portner¹, Klemens Bauer¹, Guillaume Bellec², Mathieu Luisier¹, Alexandros Emboras¹

¹Integrated Systems Laboratory, ETH Zurich, 8092 Zurich, Switzerland.

²Machine Learning Research Unit, TU Wien, 1040 Vienna, Austria.

Keywords: Dynamic Memristor, Neuromorphic, In-memory Computing, Electro-Optical Memristor, Three-factor learning, Short-term plasticity, Persistent Photoconductivity

Abstract

Modern computers perform pre-defined operations using static memory components, whereas biological systems learn through inherently dynamic, time-dependent processes in synapses and neurons. The biological learning process also relies on global signals—neuromodulators—who influence many synapses at once depending on their dynamic, internal state. In this study, using optical radiation as a global neuromodulatory signal, we investigate nanoscale SrTiO₃ (STO) memristors that can act as solid-state synapses. Via diverse sets of measurements, we demonstrate that the memristor’s photoresponse depends on the electrical conductance state, following a well-defined square root relation. Additionally, we show that the conductance decays after photoexcitation with time constants in the range of 1 – 10 s and that this effect can be reliably controlled using an electrical bias. These properties in combination with our device’s low power operation (< 1 pJ per optical pulse) and small measurement variability may pave the way for space- and energy-efficient implementations of complex biological learning processes in electro-optical hardware.

Introduction

Biological neuronal function and synaptic learning mechanisms are governed by decay processes, with a wide range of time constants that depend on the internal dynamics of neurons and synapses^{1–4}. These dynamics act as a transient memory state that has been hypothesized to help bridge the gap between synaptic and environmental timescales^{5,6}. This so called temporal credit assignment problem is one of the most challenging tasks that biological nervous systems have to solve to be able to learn through reinforcement^{5,7}. Additionally, the synaptic memory state is modulated by local neuronal activity as well as global neuromodulatory signals that influence many synapses at once⁸. These neuromodulators encode environmental cues such as e.g. reward, surprise or novelty, which are critical for the learning process in biology⁹. Integrating these signals with dynamic synapses into neuromorphic hardware could therefore improve the capabilities of bio-realistic, artificial neural networks, especially in dynamic environments¹⁰ where traditional AI approaches lack behind their biological counterpart¹¹.

One type of such neuromorphic hardware are custom complementary metal-oxide-semiconductor (CMOS) circuits, which have been employed to emulate the complex dynamic behavior of synapses and neurons¹². For instance, analog circuits based on RC elements, where a capacitor stores charges that are gradually depleted through a resistor, can realize volatile decay processes^{13–15}. Such implementations offer high controllability and rely on conventional circuit components, making hardware synthesis straightforward¹⁶. However, this approach also faces limitations, in particular the large footprint of the employed capacitors. Moreover, extending synaptic functions to support more complex plasticity mechanisms, e.g., involving neuromodulators, requires additional circuitry for each synapse, further increasing size and energy consumption. These challenges have prompted the search for alternative hardware paradigms better suited to bio-inspired learning.

Memristor-based architectures show great promise as they can inherently emulate dynamic decay processes^{17,18,19} without large capacitors or inefficient leakage currents. Memristors are two-terminal nanoscale devices that change their conductance in response to electrical stimuli²⁰, similar to how synaptic weights vary in response to neuronal spikes. Also memristors sensitive to optical signals have been proposed^{21,22}. Furthermore, studies have demonstrated that, in addition to the device’s steady-state conductance, the internal dynamics of memristors can be leveraged to replicate the biophysical processes in synapses and neurons²³. Indeed, the interplay between electronic, ionic, and thermal processes—each operating on its own energy and time scale—offers the possibility to create a range of different time constants^{24–28}. By harnessing these dynamic processes, inherent to so-called “dynamic” memristors, bio-realistic synaptic learning rules have been implemented in single devices^{24,29,30}, as well as in synaptic circuits based on memristors^{19,31,32}.

Additionally, the effect of global neuromodulatory signals on conventional (non-dynamic) memristor synapses has been investigated. For example, Sarwat et al. achieved reward-modulated learning by applying combined optical and electrical stimuli to control synaptic changes in phase-change memristive devices³³. However, due to the use of non-dynamic memristors, the temporal evolution of the internal memory state and its sensitivity to the timing of global modulatory signal delivery could not be explicitly considered. This leaves an opportunity to investigate the combination of a dynamic memristor—that is, a memristor with an evolving memory state—and its interaction with a global neuromodulatory signal. Specifically, we are looking for a space- and energy-efficient hardware implementation of synapses that not only react to local neuronal signals with a change in their memory state, but also allow for higher complexity synaptic functions, which include interactions between a global signal and local, dynamic memory states. Furthermore, the timescale of the state’s decay needs to be tuned to the dynamics of the environment or task that the neural network implements³¹. This requires close control over the temporal evolution of the memory state for each individual synapse.

In this paper, we present a dynamic memristor that realizes these functions. Namely, it (1) responds to local signals by a short-term change in its memory and then decays back (dynamic memory state), (2) is sensitive to global signals in a way that depends on that dynamically evolving local state (state-dependent global modulation), and (3) allows for exact control over

the state's temporal evolution (controllable decay time). Specifically, we fabricated two-terminal Pt/Cr – SrTiO₃ – Ti/Pt memristors, whose conductance models the synapse's dynamic memory state that interacts both with electrical (local) and optical (global) signals. In this scheme, light acts as a neuromodulator, which offers several advantages: (i) It is not limited by the RC time constant of electrical stimuli (low latency)³⁴, (ii) it can address many devices simultaneously, without complex wiring and associated peripheral circuits (small spatial footprint), and (iii) it consumes < 1pJ per optical pulse (high energy efficiency). Altogether, these features allow for the implementation of global neuromodulator stimulations on a small spatial footprint and at low energy consumption.

We go on to show that the photoresponse to the global neuromodulator depends on the memristor's conductance value (i.e., its memory state) and that the temporal dynamics of our device's conductance state can be controlled through the introduction of an electrical bias signal. Finally, we link these findings to biological learning processes, demonstrating how our device properties can be used in so called three-factor learning rules⁸. These rules could expand the capabilities of bio-realistic artificial neural networks to new tasks such as sequential learning³⁵, reinforcement learning^{36,37}, and classification in dynamic environments³⁸, potentially providing a more energy-efficient alternative to traditional neural networks³⁹. The space- and energy-efficient hardware implementation of such higher-complexity synaptic learning rules highlights the potential of our electro-optical devices as building blocks for future neuromorphic circuits.

Results and Discussion

Experimental Setup and Basic Device Working Principle

The experimental setup and device schematic are illustrated in Figure 1a. The device can be measured electrically and illuminated with UV light (light-emitting diode with $\lambda = 365$ nm) from top through an optical fiber. The memristor consists of two electrodes (Pt/Cr and Ti/Pt) that are fabricated on a single-crystal SrTiO₃ (STO) substrate. The whole device is encapsulated by a SiN layer that acts as an oxygen and moisture barrier. A FIB/SEM cross-section of the fabricated device is presented in Figure 1b. A gap of approximately 40 nm between the Pt/Cr and Ti/Pt electrodes is realized using electron-beam lithography and a lift-off process. Further details on the fabrication process can be found in Ref. [40]. The current-voltage characteristics of the device at different optical illumination intensities are shown in Figure 1c. Under dark conditions (black line), when the voltage is swept from -2V to 2V, the current exhibits the typical “eightwise” hysteresis⁴¹ of an STO memristor. This hysteresis is mainly attributed to the modulation of the Schottky barrier due to the creation and migration of oxygen vacancies (V_O^-) near the Pt/Cr/STO interface^{42,43}. When light is turned on, the current-voltage characteristics shift towards higher currents. While this light-induced increase of the electrical conductance usually disappears immediately after turning off the optical signal⁴⁴, in our devices, it only slowly decreases back to its initial value, as can be seen in Fig. 1d. In this experiment the current is measured at a constant read voltage of $V_{read} = 0.6$ V, while UV pulses

of different durations are applied. Under illumination, the current steadily increases, which leads to a higher photocurrent for longer pulses. The initial relaxation of the photocurrent (timescale of ms) is more pronounced for longer pulses, while the long-term decay (10s of seconds) is similar for all pulse widths.

Figure 1e reveals how the decay of the current under optical excitation depends on the device conductance state. As a reference, we first consider a purely electrical response (black and grey lines), where the mean (solid lines) and standard deviation (shaded area) over three measurements of the same device are reported for two distinct initial conductance states ($G_o^{(i)}$ and $G_o^{(ii)}$). In both cases, an electrical pulse with amplitude $V_{pulse} = 1.9V$ is applied during 100 ms, which leads to a conductance increase, followed by a decay during which the current is read at $V_{read} = 0.6V$. The experiment is then repeated using an optical instead of an electrical pulse (optical pulse with $P_{opt} = 65\text{mWcm}^{-2}$ and a duration of 100 ms; purple curves). For the $G_o^{(i)}$ state, the electrical and optical responses exhibit a very similar time decay. However, for the $G_o^{(ii)}$ state, the conductance is significantly higher in the optical than in the electrical case immediately after the pulse.

The origin of electrically-induced conductance decay in STO-based memristors is a topic of active research, possibly involving different physical mechanisms: It has been attributed to (i) the back-migration of oxygen vacancies toward the Pt-STO interface and subsequent filling of vacancies by oxygen incorporation^{45,46}, (ii) the slow release of trapped charges⁴⁷, or (iii) a combination of both effects⁴⁸. Purely electrical measurements are not sufficient to unambiguously determine the phenomena governing the observed conductance decay as measured data can be fitted with both oxygen vacancy migration and trapping/detrapping models^{49,50}. Nevertheless, experimental evidence has been accumulating that underlines the sensitivity of the conductance decay on the oxygen partial pressure during measurement^{46,51}, the presence of oxygen blocking layers^{52,53}, and the oxygen permeability of the top electrode³⁰. Furthermore, the generation of oxygen vacancies upon electrical stimuli has been experimentally verified through electron energy-loss spectroscopy⁴². Such experiments support an ionic origin of the conductance decay rather than a pure trapping / detrapping mechanism, at least for sufficiently high pulse voltages.

The similarity between the optical and electrical responses of $G_o^{(i)}$ in Fig. 1e suggests that their decay behavior depends on the same mechanism. Based on the previous discussion, this mechanism could be: (1) the generation and subsequent back-filling of oxygen vacancies with oxygen or (2) charge trapping and subsequent slow release of trapped carriers. Indeed, long relaxation times have been observed for the photoresponse of STO. They have been attributed to interface charge trapping⁵⁴, trapping at bulk defects^{55,56}, or light-induced generation of oxygen vacancies^{57,58}. While UV-light-induced generation of oxygen vacancies in STO has, to our knowledge, only been reported at higher optical intensities than in our work (2.4 W/cm^2 compared to our 96 mW/cm^2)⁵⁸, experiments with Au-TiO₂ systems demonstrated the generation of oxygen vacancies at UV light intensities of only 2 mW/cm^2 from a 365nm LED light source at room temperature⁵⁹. While the electronic and electrochemical properties of TiO₂ and STO are different, reported formation energies of oxygen vacancies at the material surface

are similar (3.1-3.7 eV⁶⁰ and 2-3 eV⁶¹ for TiO₂ and STO, respectively). Furthermore, for both metal oxide systems (Au-TiO₂⁶² and Pt-STO^{43,63}) the formation energy has been observed to decrease significantly in the proximity of the high work-function metals, making the light assisted generation of oxygen vacancies at these interfaces feasible. On the other hand, charge trapping has also been shown to lead to persistent photoconductivity in STO, but experimental⁵⁶ and theoretical⁶⁴ works have traced back the origin of this phenomenon to substitutional hydrogen defects, which form only under high temperature annealing (420 – 1200 °C), in the presence of hydrogen-containing compounds^{56,65}. By contrast, analyzing the UV photoresponse of various untreated, commercially available single-crystal STO substrates revealed no persistent photoconductivity⁶⁶, effectively ruling out trapping at bulk defects (e.g. due to impurities) as an explanation for the prolonged decay of the photoresponse in our devices. Nevertheless, it is conceivable that interface defects (intrinsic or introduced during fabrication) could form trap states affecting the photoresponse.

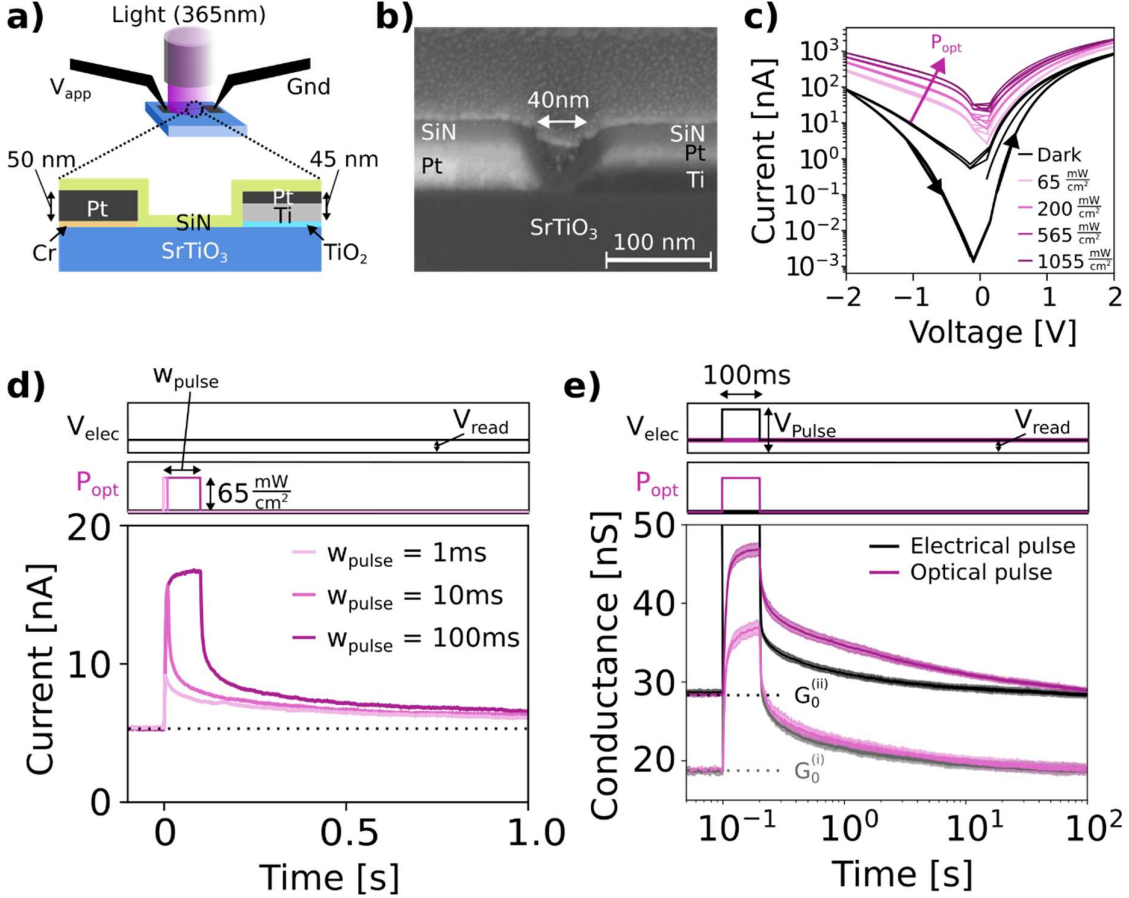


Figure 1: Experimental setup, device design and basic characterization of our Pt/Cr – SrTiO₃ – Ti/Pt memristor. (a) Schematic illustration of the experimental setup and of the device stack. Free-space illumination at a wavelength of $\lambda = 365$ nm is focused on the active region of our two-terminal STO-based memristive device. A voltage can be applied to the Pt/Cr electrode, whereas the Ti/Pt one is grounded. (b) Cross-sectional SEM image of the memristor gap. The topmost material is a protective Pt layer. It is used to fabricate the cross-sectional slice, but is not part of the device itself. (c) IV characteristics of the device, measured in the dark (black lines) and under varying light intensities (P_{opt} , indicated by shaded purple regions). (d) Current as a function of time measured at a constant read voltage $V_{\text{read}} = 0.6$ V. At $t=0$ optical pulses with a power of 65 mW cm^{-2} and different widths are applied. (e) Conductance as a function of time under the application of both electrical (black lines) and optical (purple lines) pulses at two different initial conductance states ($G_0^{(i)}$ and $G_0^{(ii)}$). The solid lines denote the mean of 3 measurements and the shaded area around the lines corresponds to the standard deviation.

Conductance-dependent Photoresponse

To further investigate the conductance-dependent photoresponse of our memristor, we illuminate it with UV pulses (1 ms, $P_{\text{pulse}} = 65 \text{ mW/cm}^2$) before and after an electrical SET at $t=0$ (Fig. 2a), while measuring the conductance at a read voltage of $V_{\text{read}} = 0.6$ V. During the SET procedure a train of 100 electrical pulses is applied ($V_{\text{SET}} = 4$ V, 1 ms). The electrical and optical protocol are shown at the top of the sub-plot, the measured conductance being plotted at the bottom. Two measurements are displayed that differ in the timing of the UV pulses after SET (light and dark blue curves). The conductance measurement begins with a slow transient phase that lasts until $t=400$ s, when the first optical pulse is applied in both measurements. A short-term conductance increase is observed whenever the device is illuminated, followed by a slow decay back to the initial value. The near-perfect overlap of the

two measured conductance traces over the first 500s shows the low measurement variability of our device. Furthermore, the optical energy consumption per pulse is estimated to be 0.37 pJ (see Supplementary Section S1), assuming a crossbar array architecture with a realistic device pitch area of $0.5625 \mu\text{m}^2$, as demonstrated in Ref. [67]. The electrical power consumed during the read operation at $V_{read}=0.6$ V ranges between 2 and 22 nW, depending on the conductance state. Additional electrical measurements of the same device confirm a low cycle-to-cycle variability⁴⁰.

After the electrical SET, the conductance increases roughly by a factor of $6\times$ (see Fig. 2b), with a subsequent decay in the timescale of several 100's of seconds. This long-term change in conductance enables us to compare the photoresponse at various conductance states corresponding to different measurement segments, labeled (1), (2), and (3). Figure 2c highlights these three segments for one of the two measurements (measurement 2). Each of the segments starts at a distinct initial (transient) conductance state ($G_0^{(1)}$, $G_0^{(2)}$, and $G_0^{(3)}$), which leads to different photoresponses ($\Delta G^{(1)}$, $\Delta G^{(2)}$, and $\Delta G^{(3)}$) under optical excitation. The following trend is observed: the larger the conductance state, the larger the photoresponse. As the conductance of the device naturally decreases over time, the strength of the photoresponse also decreases as the UV pulse is delayed with respect to the electrical SET. In other words, the closer an optical pulse occurs to the SET event, the larger the resulting photoresponse. This timing dependence enables the implementation of transient memories of past activity that persist until a reward signal (optical pulse) arrives. Such transient memories are a critical element of three-factor learning rules, as they allow synapses to link local events with delayed global feedback⁵.

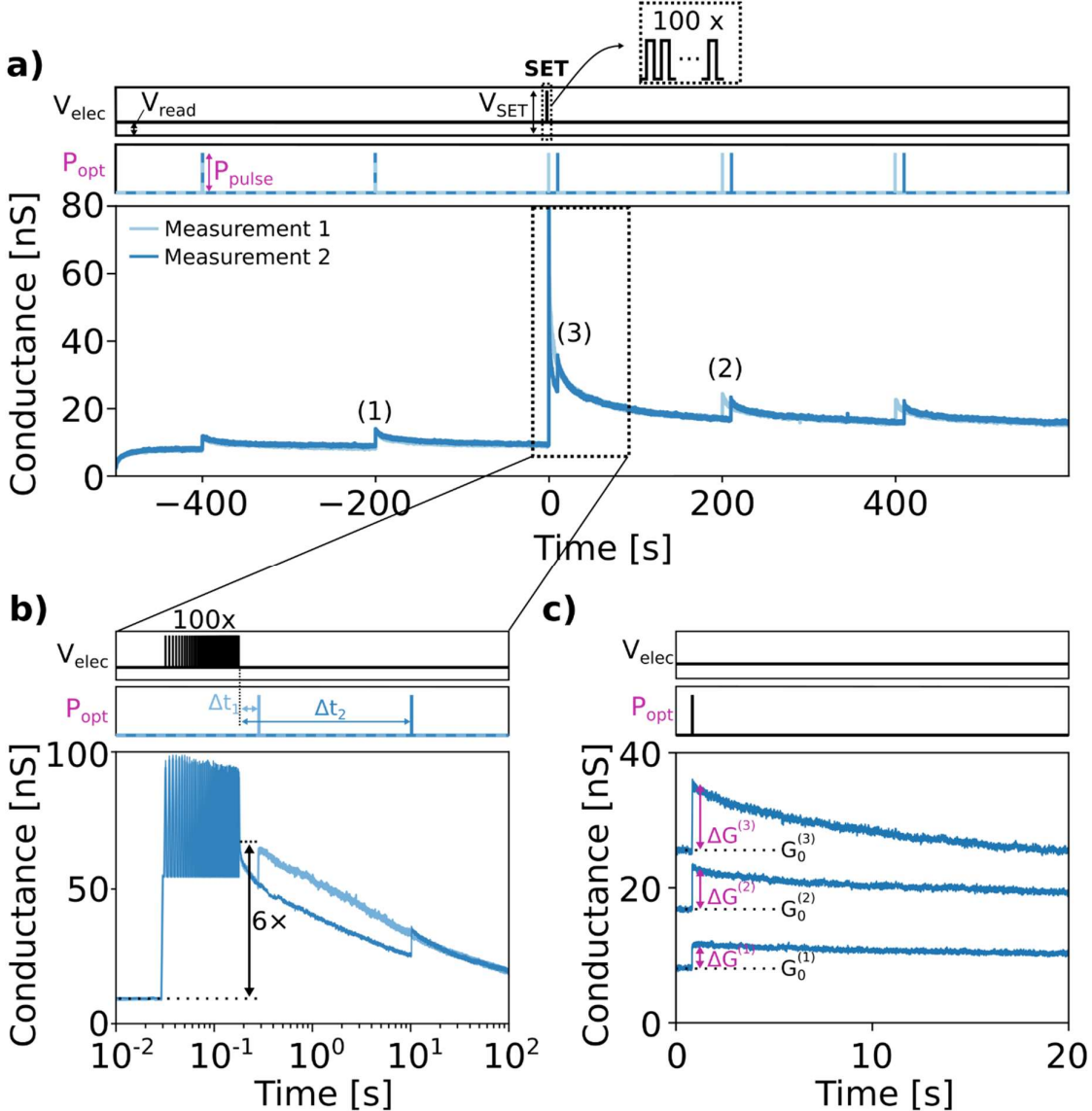


Figure 2: Characterization of the electrically and optically induced conductance change of our STO dynamic memristor. For each measurement the electrical protocol (V_{elec}) and the applied optical power (P_{opt}) are shown in the top two panels of each subfigure. (a) Two separate measurements (light and dark blue) of the conductance vs. time characteristics differing in the timing of the applied UV pulses after electrical SET (see the protocol on top). (b) Zoom-in of the measurement region in the dotted rectangle plotted on a logarithmic x-axis. The timing difference of the optical pulses with respect to the end of the electrical SET are $\Delta t_1 = 0.1$ s and $\Delta t_2 = 10$ s for measurement 1 and 2 respectively. (c) Plot of the measurement parts labelled (1), (2) and (3) in (a). The initial conductance state $G_0^{(1,2,3)}$ before the arrival of an optical pulse and the photoresponse $\Delta G^{(1,2,3)}$ are indicated.

Besides the state-dependent (or timing-dependent) magnitude of the photoresponse, its temporal evolution and its controllability are of great interest as they can be leveraged in a wide range of synaptic learning rules^{8,30,68,69} and machine learning algorithms^{70,71}. To this end, we execute the measurement protocol shown in Figure 3a (top panel) and report the resulting conductance in its bottom panel. Here, contrary to the measurement in Fig. 2a, we do not set a constant read voltage, but instead read pulses (0.5 ms, $V_{read} = 0.6$ V) with a variable bias voltage in-between (1.5 ms, V_{bias}). This protocol allows to read out the conductance at a fixed

voltage (V_{read}), while simultaneously changing the time-averaged voltage applied to the device ($\overline{V_{app}} = (0.5 \cdot V_{read} + 1.5 \cdot V_{bias})/2$), with V_{bias} as control parameter. We can thus observe the decay behavior for different $\overline{V_{app}}$ in distinct measurements, while still reading out the conductance in a consistent way (i.e., at the same voltage) for all measurements. The effect of the bias voltage on the conductance is threefold: (1) During the initial transient phase ($t < -400$ s) the conductance increases for $\overline{V_{app}} > 0$ (i.e., at a bias of 0 V and 0.6 V) and decreases for $\overline{V_{app}} < 0$ (at a bias of -0.6 V). The conductance change is larger for larger values of $\overline{V_{app}}$. (2) The decay of the conductance state $G_0(t)$ after the electrical SET ($t > 0$) is influenced by the bias voltage (a higher V_{bias} leads to a slower decay). Finally, (3) the decay after the optical pulses is similarly affected.

We first focus on the decay after the SET, i.e., the electrically-induced conductance change. It can be fitted by combining one exponential and one stretched exponential function (dashed black line in Fig. 3a). This SET decay model is also shown in the inset as a log-log plot. Its behavior is captured by the following equation

$$G_0(t) = G_{steady} + \frac{\Delta G^{(SET)}}{\gamma^{(SET)} + 1} \cdot \left(\gamma^{(SET)} * \exp\left(-\frac{t - t_0}{\tau_1^{(SET)}}\right) + \exp\left(-\left(\frac{t - t_0}{\tau_2^{(SET)}}\right)^\beta\right) \right). \quad (1)$$

Here, G_{steady} is the initial conductance state before the SET pulses, $\Delta G^{(SET)}$ denotes the difference in conductance between G_{steady} and right after the SET pulses (i.e., the conductance increase), $\gamma^{(SET)}$ is a fitting parameter that weights the relative strength of the first and second exponential, β is the stretching exponent, $\tau_1^{(SET)}$ and $\tau_2^{(SET)}$ are time constants, and t_0 corresponds to the time immediately after the electrical SET pulses. The values for the parameters are given in Supplementary Section S2. The SET decay involves at least two time constants: a small one dominating at the beginning of the decay process ($\tau_1^{(SET)}$) and a larger one for the remainder ($\langle \tau_2^{(SET)} \rangle$). Therein, $\langle \tau_2^{(SET)} \rangle$ refers to the mean time-constant of the stretched exponential function. It is defined as

$$\langle \tau_2^{(SET)} \rangle = \frac{\tau_2^{(SET)}}{\beta} \cdot \Gamma\left(\frac{1}{\beta}\right) \quad (2)$$

where $\Gamma(\cdot)$ represents the mathematical gamma function. Similar fitting models have been reported in the literature for the conductance decay in STO and other oxide memristors, including stretched exponentials^{72,73} and a combination of exponentials^{45,74,75}. Also, power laws have been proposed^{47,76} as well as combinations of stretched exponentials with different time constants⁷⁷ or power laws and exponentials⁵⁰.

As a second step we characterize the decay after the optically induced conductance change at different bias voltages. It can be observed in the zoom-in of the optical pulses at $t=200$ s in the dotted rectangle (Fig. 3b). Before these pulses, the conductance reaches a steady state for all

three measurements ($G_0(t) = G_{\text{steady}}^{(V_{\text{bias}})}$), allowing for the observation of the relaxation dynamics of the photoresponse ($G_{\text{opt}}(t)$) at a stable conductance state. The purple dashed lines corresponds to a fit with a double exponential model and two time constants $\tau_1^{(\text{opt})}$ and $\tau_2^{(\text{opt})}$

$$G_{\text{opt}}(t) = G_0(t) + \frac{\Delta G^{(\text{opt})}}{\gamma^{(\text{opt})} + 1} \cdot \left(\gamma^{(\text{opt})} * \exp\left(-\frac{t - t_0}{\tau_1^{(\text{opt})}}\right) + \exp\left(-\frac{t - t_0}{\tau_2^{(\text{opt})}}\right) \right) \quad (3)$$

The values of all parameters can be found in the supplementary material. The electrical and optical time constants are plotted as a function of the bias voltage in Fig. 3c, indicating that the time constants increase at larger V_{bias} . We have thus shown that it is possible to control the decay timescale of both electrically and optically induced conductance changes through the application of an external bias voltage.

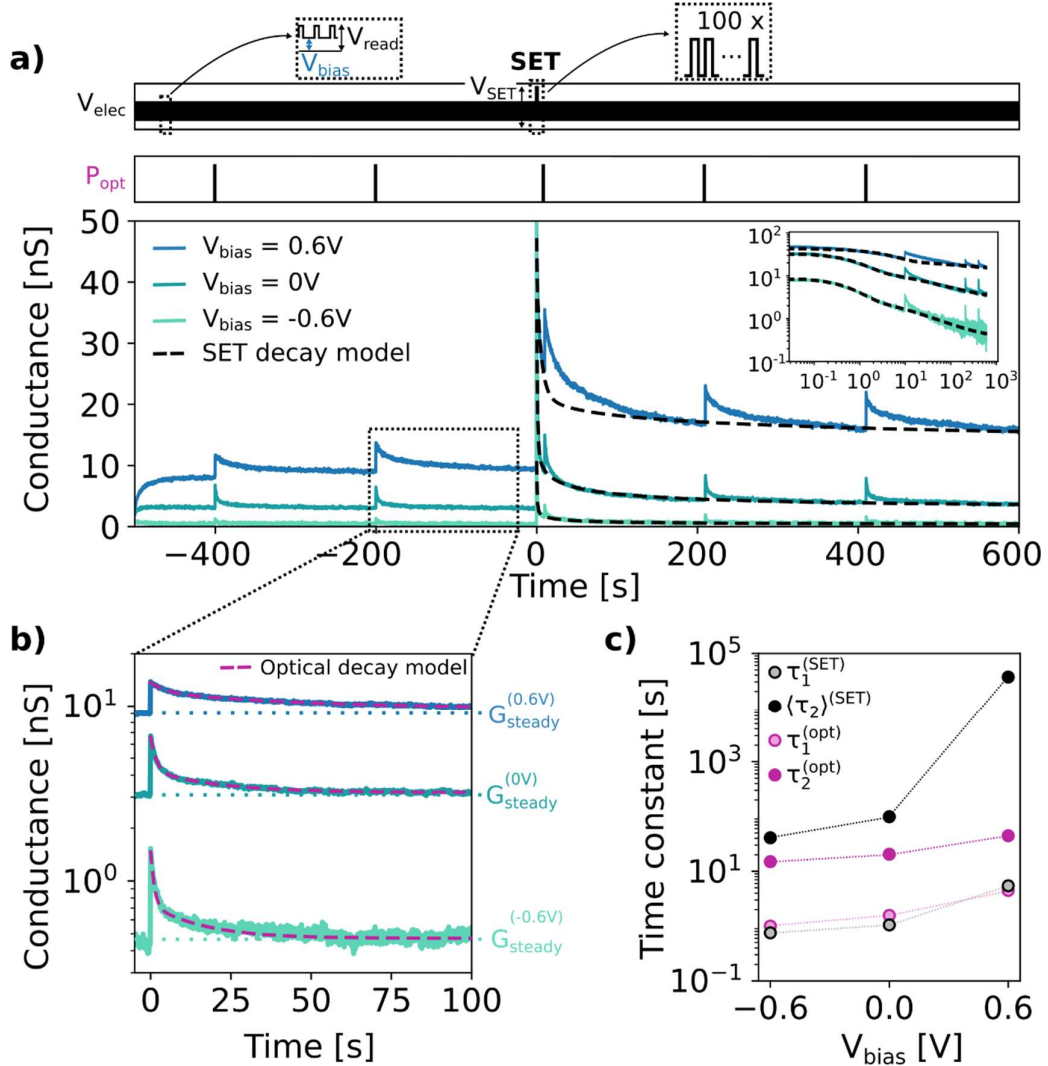


Figure 3: Controllability of the conductance decay rate after the application of electrical and optical pulses. (a) (Top) Applied voltage protocol using 0.6V (0.5ms) read pulses and a variable bias voltage in-between (1.5ms). A train of 100 SET pulses (4V, 1ms) is applied at $t=0$. The applied optical pulses (1ms, 65mW/cm²) are shown in the panel below. (Bottom) Conductance values at $V_{read} = 0.6V$ for three different bias voltages (V_{bias}). The relaxation after the SET is fitted for each V_{bias} with the decay model in Eq. (1) (dashed black lines). The inset shows the same data for $t > 0$ on a log-log plot. (b) Zoom-in of the area marked by the dotted rectangle in (a). The three different initial conductance states ($G_{steady}^{(V_{bias})}$) are labelled and the relaxation of the photoresponse is fitted with the optical decay model in Eq. (3) (purple dashed lines). (c) Extracted decay time constants from the SET and optical decay models as a function of V_{bias} . The dashed lines serve as guides to the eye.

Finally, to determine the dependence of the photoresponse $\Delta G^{(opt)}$ with respect to the device conductance G_0 , we report both quantities in Fig. 4a for a large set of measurements. Two different SET protocols were used: one employing single electrical pulses to SET the device and one where a train of 100 pulses is applied (see supplementary section S3 for details). In Fig. 4a, the markers' color denotes the time interval between the electrical SET and the subsequent UV pulse, while their shape distinguishes different bias regimes. As indicated by the dashed line, the photoresponse $\Delta G^{(opt)}$ increases with G_0 , with the exception of a few outliers (dotted ellipses). Apart from these outliers the relation between $\Delta G^{(opt)}$ and G_0 follows a power law:

$$\Delta G^{(opt)} = G_0^k \quad (4)$$

with an exponent $k = 0.50$ (i.e., a square root relation). Neither the applied protocol (marker size), the UV pulse timing with respect to the electrical SET (color), nor the applied bias voltage (marker symbol) affect the observed power law. We therefore conclude that the conductance state of the device (G_0) is the main predictor for the magnitude of the photoresponse ($\Delta G^{(opt)}$). Figure 4(b) shows the photoresponse as a function of the optical power for a predefined conductance state. We observe larger ΔG at higher optical power, with a power law exponent $k = 0.52$.

Bio-inspired Learning Rules

The conductance-dependent photoresponse is an interesting feature that advanced neuromorphic computing circuit might take advantage of. It enables the translation of a global (optical) signal, impinging on many devices simultaneously in a crossbar array, into a local (electrical) response that differs from device to device depending on their internal memory state (Figure 4c). Furthermore, this state decays with a specific time constant that can be controlled electrically, effectively implementing a voltage-tunable temporal filter that weights the photoresponse: The closer the optical signal arrives to an electrical pulse the higher the response.

The combination of these features, i.e., (1) dynamic memory state, (2) state-dependent global modulation, and (3) controllable decay time, is crucial for complex synaptic plasticity models, such as bio-inspired three-factor learning rules⁸. One example of such a rule is reward-modulated spike timing dependent plasticity (R-STDP), which governs how the synaptic

weight (w_t) is updated according to its local pre- and postsynaptic inputs (*pre* and *post*) and to a global neuromodulatory reward signal (δ_t):

$$w_t = w_{t-1} + \Delta w_t(\text{pre}, \text{post}, \delta_t). \quad (5)$$

In real world environments the global reward signal arrives much later than the local neuronal activity (*pre*, *post*) that led to the rewarded behavior. To bridge this temporal gap it is crucial that synapses hold a local transient memory of previous activity with timescales adapted to the specific environment. This memory is called eligibility trace (z_t) and is computed according to:

$$z_t = \lambda z_{t-1} + h_t(\text{pre}, \text{post}), \quad (6)$$

where $\lambda \in [0,1]$ denotes the decay rate (i.e., timescale) of the eligibility trace and $h_t(\text{pre}, \text{post})$ the two-factor STDP update⁸. As long as the eligibility trace is nonzero, the synapse is eligible for a weight update. Hence, when a reward signal δ_t arrives, the weight gets updated according to:

$$\Delta w_t = \alpha \delta_t \cdot z_t, \quad (7)$$

where α denotes the learning rate⁸.

The eligibility trace (Eq. 6) and the calculation of the weight update (Eq. 7), can be approximated in our hardware as follows: The intrinsically decaying conductance state (G_0) models the local synaptic eligibility that is modified by an electrical signal (V_{pulse}), which represents $h_t(\text{pre}, \text{post})$. With a bias voltage (V_{bias}) the decay time constant (λ) of G_0 can be controlled (see Fig. 3c). The UV light intensity (P_{opt}) then corresponds to the reward signal, while the conductance-dependent photoresponse ΔG implements the processing of the reward. This calculation is visualized in Fig. 4d and the correspondence between the learning algorithm and device properties is summarized in Table 1.

Theory	Device
w_t	-
h_t	V_{pulse}
$\alpha \delta_t$	$\sqrt{P_{opt}}$
z_t	$\sqrt{G_0}$
λ	V_{bias}
Δw_t	ΔG

Table 1: Correspondence between three-factor learning in Eqs. (5)-(7) and our device properties.

It should, however, be noted that our devices are not yet fully capable of implementing the function of biological synapses in a three-factor learning model (see Table 2). In particular, to fully implement the R-STDP rule, the synapse model requires two distinct states: the non-volatile synaptic weight w_t , and a hidden eligibility z_t . While our devices can implement controllable, short-term memory traces that interact with a global neuromodulatory signal, they do not exhibit a second, fully non-volatile state. Addressing this issue requires an in-depth understanding of the physical mechanisms governing the switching of our STO memristors, which will enable us to engineer next-generation components appropriately. Our measurements of the optical decay under different bias voltages (Fig. 3b) suggest that the volatility can be controlled in principle. Moreover, studies have shown that the introduction of oxygen blocking layers^{52,53} or electrodes³⁰ may lead to non-volatile (electrical) operation in practice. These experiments indicate that a non-volatile optical response could be possible, but additional work going beyond the scope of this paper will be needed to reach this point.

Synaptic function	Implemented by our devices
(1) Dynamic memory state	✓
(2) State-dependent global modulation	✓
(3) Controllable decay time	✓
(4) Stable (non-volatile) weight	✗

Table 2: Synaptic functions required for three-factor learning

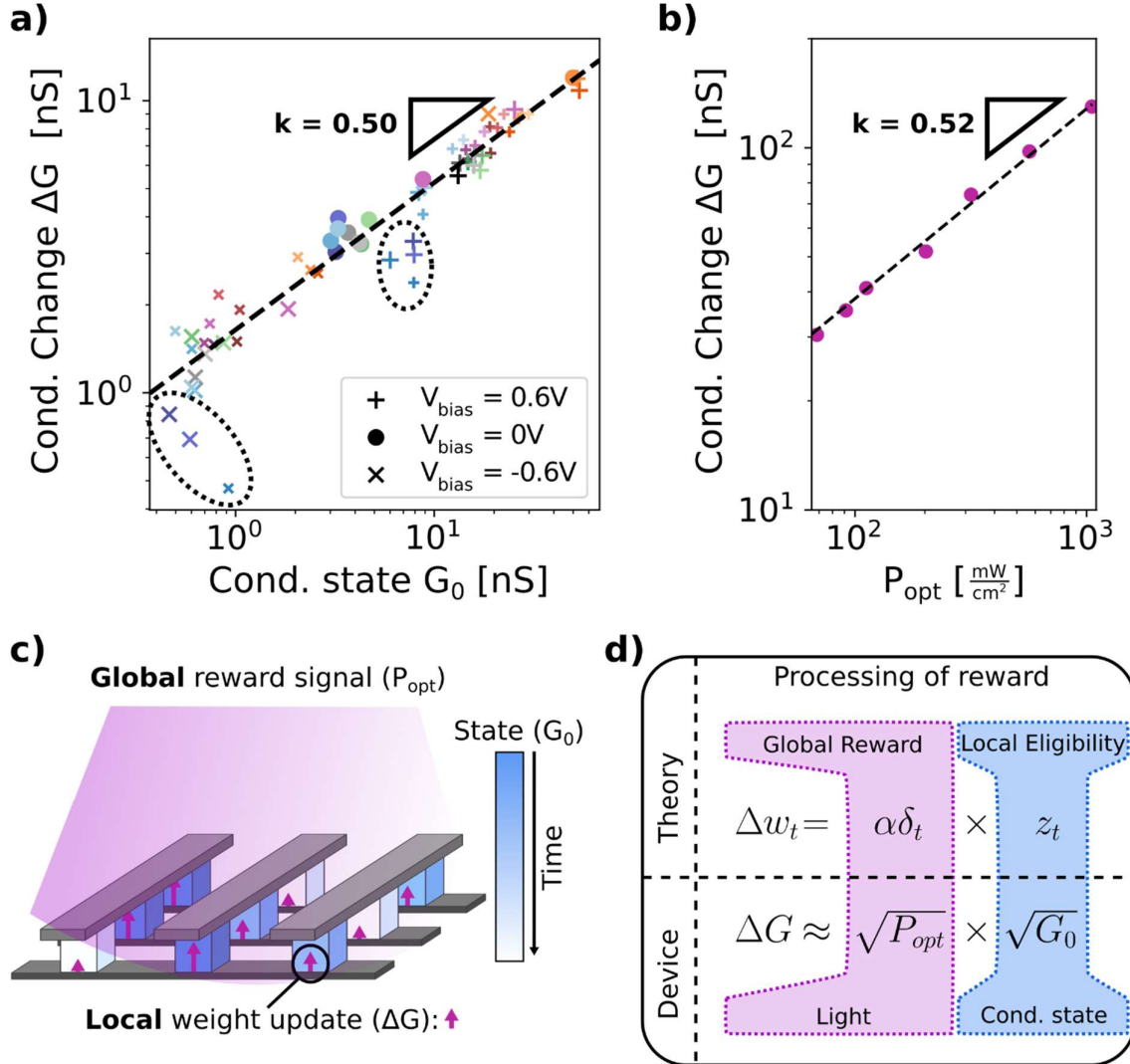


Figure 4: Summary of the photoresponse features and possible application of our STO devices in three-factor learning algorithms. (a) Optically induced conductance change $\Delta G^{(opt)}$ as a function of the conductance state G_0 for all measurements performed in this work. The dotted ovals mark outliers, whereas the dashed black line is a power law fit (exponent $k=0.50$) of the data without the outliers. Marker shape corresponds to V_{bias} , marker size to the employed measurement protocol and marker color to the timing relative to the SET pulse (see Supplementary Section S3 for details). (b) $\Delta G^{(opt)}$ as a function of the optical power P_{opt} . The dashed black line is a power law fit (exponent $k=0.52$). (c) Artistic rendering of a possible hardware implementation of crossbar arrays with individual devices exhibiting different conductance states (eligibility, G_0). A global optical signal illuminated from top is envisioned to trigger local conductance updates that depend on G_0 . (d) Computation of the theoretical weight update Δw_t (upper part; labelled “Theory”) and the mathematical formulation of the conductance-dependent photoresponse (ΔG) extracted from our device (bottom part; labelled “Device”).

Conclusion and Outlook

In this work we demonstrated SrTiO_3 -based electro-optical memristors that integrate several essential synaptic functions relevant for three-factor learning rules and other emerging neuromorphic applications: (1) a local transient memory state that (2) interacts with a global

optical signal producing a state-dependent photoresponse and (3) whose temporal evolution is controllable.

Specifically, we showed that the device changes its internal conductance state upon optical or electrical excitation and then relaxes back toward its initial state with characteristic time constants ranging from milliseconds to hundreds of seconds (transient memory). These decay times can be tuned by applying a bias voltage, enabling the matching of the memory state's time-constant to specific tasks. Crucially, the steadily decaying local conductance state influences the device's electrical response to a global optical signal: the larger the conductance state, the stronger the photoresponse, according to a well-defined square-root relation. In other words, because the conductance decays over time, optical signals that arrive earlier produce stronger photo-responses, effectively making the local electrical response sensitive to the timing of the global optical signal. This timing-dependent global-to-local conversion is central to three-factor learning rules, which are considered to be an important mechanism in biological learning. Finally, all these functions are achieved within a nanoscale footprint and at very low energy cost, meeting critical requirements for scalable neuromorphic hardware architectures.

Looking forward, two complementary research directions can be envisioned. On the device level, advancing the physical understanding of oxygen vacancy dynamics and trapping processes will be key to tailoring the balance between volatile and non-volatile operation. At a systems level, integrating STO memristors into crossbar arrays and testing them in hardware-implemented learning tasks will clarify their potential for bio-realistic computing. Together, these efforts could position electro-optical memristors as a compact and versatile platform enabling the implementation of complex learning functions in next-generation neuromorphic hardware.

Contributions

C.W. developed the concept of the paper, fabricated and measured devices. He wrote the paper with input from all co-authors. H.H. provided the SEM cross section image. M.M. helped with the identification of the physical mechanism in the devices. T.Z. supported the development of the characterization setup and device measurements. K.P. assisted with fabrication. K.B. helped with writing. G.B assisted with the bio-inspired learning algorithms and writing. M.L. supervised the project, gave inputs on the device working principle and helped with the writing and structuring of the paper. A.E. supervised the project and led the study with inputs on numerous topics including the fabrication/characterization of the devices and the writing of the paper. C.W. and A.E. conceived the project.

Corresponding author

Correspondence to Christoph Weilenmann

Acknowledgement

We would like to thank the Operations Team of the Binnig and Rohrer Nanotechnology Center, especially Antonis Olziersky, Roland Grundbacher, Ute Drechsler, Michael Stiefel, Steffen Reidt and Diana Davila for their continued help and sharing of their fabrication knowledge. Funding from the Werner Siemens Foundation (A.E., M.L., and M.M.), the SNSF Strategic Japanese-Swiss Science and Technology Program under project metacross (grant number 214068, C.W. and A.E.), the SNSF Sinergia project ALMOND (grant number 198612, M.L., and T.Z.), and the SNSF Advanced Grant project QuaTrEx (grant number 209358, M.L.) is acknowledged.

References

1. Gerstner, W., Lehmann, M., Liakoni, V., Corneil, D. & Brea, J. Eligibility Traces and Plasticity on Behavioral Time Scales: Experimental Support of NeoHebbian Three-Factor Learning Rules. *Front. Neural Circuits* **12**, 1–16 (2018).
2. Nadim, F. & Manor, Y. The role of short-term synaptic dynamics in motor control. *Curr. Opin. Neurobiol.* **10**, 683–690 (2000).
3. Citri, A. & Malenka, R. C. Synaptic plasticity: multiple forms, functions, and mechanisms. *Neuropsychopharmacology* **33**, 18–41 (2008).
4. Shimizu, G., Yoshida, K., Kasai, H. & Toyoizumi, T. Computational roles of intrinsic synaptic dynamics. *Curr. Opin. Neurobiol.* **70**, 34–42 (2021).
5. Legenstein, R., Pecevski, D. & Maass, W. A learning theory for reward-modulated spike-timing-dependent plasticity with application to biofeedback. *PLoS Comput. Biol.* **4**, (2008).
6. Kobayashi, S. & Schultz, W. Influence of reward delays on responses of dopamine neurons. *J. Neurosci.* **28**, 7837–7846 (2008).
7. Sutton, R. S. *Temporal credit assignment in reinforcement learning*. (University of Massachusetts Amherst, 1984).
8. Frémaux, N. & Gerstner, W. Neuromodulated spike-timing-dependent plasticity, and theory of three-factor learning rules. *Front. Neural Circuits* **9**, (2015).
9. Avery, M. C. & Krichmar, J. L. Neuromodulatory systems and their interactions: A review of models, theories, and experiments. *Front. Neural Circuits* **11**, 1–18 (2017).
10. Doya, K. Metalearning and neuromodulation. *Neural Networks* **15**, 495–506 (2002).
11. Zador, A. *et al.* Catalyzing next-generation Artificial Intelligence through NeuroAI. *Nat. Commun.* **14**, 1–7 (2023).
12. Kaiser, J. *et al.* Emulating dendritic computing paradigms on analog neuromorphic hardware. *Neuroscience* **489**, 290–300 (2022).
13. Cruz-Albrecht, J. M., Yung, M. W. & Srinivasa, N. Energy-efficient neuron, synapse and STDP integrated circuits. *IEEE Trans. Biomed. Circuits Syst.* **6**, 246–256 (2012).
14. Joubert, A., Belhadj, B., Temam, O. & Héliot, R. Hardware spiking neurons design: Analog or digital? *Proc. Int. Jt. Conf. Neural Networks* 6–10 (2012) doi:10.1109/IJCNN.2012.6252600.
15. Gopalakrishnan, R. & Basu, A. Triplet Spike Time Dependent Plasticity: A floating-gate Implementation. 1–13 (2015).
16. Frenkel, C. & Indiveri, G. ReckOn: A 28nm sub-mm² task-agnostic spiking recurrent neural network processor enabling on-chip learning over second-long timescales. in *2022 IEEE International Solid-State Circuits Conference (ISSCC)* vol. 65 1–3 (IEEE, 2022).
17. Jo, S. H. *et al.* Nanoscale Memristor Device as Synapse in Neuromorphic Systems.

Nano Lett. (2010) doi:10.1021/nl904092h.

- 18. Ricci, S., Kappel, D., Tetzlaff, C., Ielmini, D. & Covi, E. Tunable synaptic working memory with volatile memristive devices. *Neuromorphic Comput. Eng.* **3**, 44004 (2023).
- 19. Demirag, Y. *et al.* PCM-trace: Scalable synaptic eligibility traces with resistivity drift of phase-change materials. *Proc. - IEEE Int. Symp. Circuits Syst.* **2021-May**, (2021).
- 20. Waser, R. *Nanoelectronics and information technology: advanced electronic materials and novel devices*. (John Wiley & Sons, 2012).
- 21. Portner, K. *et al.* Analog Nanoscale Electro-Optical Synapses for Neuromorphic Computing Applications. *ACS Nano* **15**, 14776–14785 (2021).
- 22. Emboras, A. *et al.* Atomic Scale Photodetection Enabled by a Memristive Junction. *ACS Nano* **12**, (2018).
- 23. Kumar, S., Wang, X., Strachan, J. P., Yang, Y. & Lu, W. D. Dynamical memristors for higher-complexity neuromorphic computing. *Nat. Rev. Mater.* **7**, 575–591 (2022).
- 24. Kim, S. *et al.* Experimental demonstration of a second-order memristor and its ability to biorealistically implement synaptic plasticity. *Nano Lett.* **15**, 2203–2211 (2015).
- 25. Mikheev, V. *et al.* Ferroelectric second-order memristor. *ACS Appl. Mater. Interfaces* **11**, 32108–32114 (2019).
- 26. Kumar, S., Williams, R. S. & Wang, Z. Third-order nanocircuit elements for neuromorphic engineering. *Nature* **585**, 518–523 (2020).
- 27. Zidan, M. A., Jeong, Y. & Lu, W. D. Temporal learning using second-order memristors. *IEEE Trans. Nanotechnol.* **16**, 721–723 (2017).
- 28. Bhattacharya, T., Bezugam, S. S., Pande, S., Wlazlak, E. & Strukov, D. ReRAM-Based NeoHebbian Synapses for Faster Training-Time-to-Accuracy Neuromorphic Hardware. in *2023 International Electron Devices Meeting (IEDM)* 1–4 (IEEE, 2023).
- 29. Yang, R. *et al.* Synaptic Suppression Triplet-STDP Learning Rule Realized in Second-Order Memristors. *Adv. Funct. Mater.* **28**, 1–10 (2018).
- 30. Xiong, J. *et al.* Bienenstock, Cooper, and Munro Learning Rules Realized in Second-Order Memristors with Tunable Forgetting Rate. *Adv. Funct. Mater.* **29**, 1–8 (2019).
- 31. Chicca, E. & Indiveri, G. A recipe for creating ideal hybrid memristive-CMOS neuromorphic processing systems. *Appl. Phys. Lett.* **116**, (2020).
- 32. Tang, Y., Levin, J. A., Aparin, V. & Rangan, V. Methods and systems for three-memristor synapse with stdp and dopamine signaling. (2012).
- 33. Sarwat, S. G., Moraitis, T., Wright, C. D. & Bhaskaran, H. Chalcogenide optomemristors for multi-factor neuromorphic computation. *Nat. Commun.* **13**, 2247 (2022).
- 34. Emboras, A. *et al.* Opto-electronic memristors: Prospects and challenges in neuromorphic computing. *Appl. Phys. Lett.* **117**, (2020).
- 35. Kirkpatrick, J. *et al.* Overcoming catastrophic forgetting in neural networks. *Proc. Natl. Acad. Sci. U. S. A.* **114**, 3521–3526 (2017).
- 36. Portner, K. *et al.* Actor-critic networks with analogue memristors mimicking reward-based learning. (2024).
- 37. Mozafari, M., Kheradpisheh, S. R., Masquelier, T., Nowzari-Dalini, A. & Ganjtabesh, M. First-spike-based visual categorization using reward-modulated STDP. *IEEE Trans. Neural Networks Learn. Syst.* (2018) doi:10.1109/TNNLS.2018.2826721.
- 38. Moraitis, T., Sebastian, A. & Eleftheriou, E. Short-term synaptic plasticity optimally models continuous environments. (2020).
- 39. Sarwat, S. G., Kersting, B., Moraitis, T., Jonnalagadda, V. P. & Sebastian, A. Phase Change Memtransistive Synapse. 1–11 (2021).
- 40. Weilenmann, C. *et al.* Single neuromorphic memristor closely emulates multiple

synaptic mechanisms for energy efficient neural networks. *Nat. Commun.* **15**, 6898 (2024).

- 41. Sarantopoulos, A., Waser, R. & Dittmann, R. Eightwise switching mechanism in memristive SrTiO₃ devices and its implications on the device performance. *Phys. status solidi* **221**, 2300483 (2024).
- 42. Cooper, D. *et al.* Anomalous Resistance Hysteresis in Oxide ReRAM: Oxygen Evolution and Reincorporation Revealed by In Situ TEM. *Adv. Mater.* **29**, 1–8 (2017).
- 43. Mladenovic, M., Kaniselvan, M., Weilenmann, C., Emboras, A. & Luisier, M. Termination-Dependent Resistive Switching in SrTiO₃ Valence Change Memory Cells. *ACS Appl. Electron. Mater.* **7**, 2839–2847 (2025).
- 44. Yasunaga, H. & Nakada, I. Photoconduction of strontium titanate. *J. Phys. Soc. Japan* **22**, 338 (1967).
- 45. Hellwig, J. *et al.* Resolving the Relaxation of Volatile Valence Change Memory. *Adv. Electron. Mater.* **2400062**, 1–12 (2024).
- 46. Baeumer, C. *et al.* Verification of redox-processes as switching and retention failure mechanisms in Nb:SrTiO₃/metal devices. *Nanoscale* **8**, 13967–13975 (2016).
- 47. Bourim, E. M., Kim, Y. & Kim, D.-W. Interface State Effects on Resistive Switching Behaviors of Pt/Nb-Doped SrTiO₃ Single-Crystal Schottky Junctions. *ECS J. Solid State Sci. Technol.* **3**, N95–N101 (2014).
- 48. Zhao, B., Xiao, M. & Zhou, Y. N. Synaptic learning behavior of a TiO₂ nanowire memristor. *Nanotechnology* **30**, (2019).
- 49. Gwon, M., Lee, E., Sohn, A., Bourim, E. M. & Kim, D. W. Doping-level Dependences of Switching Speeds and the Retention Characteristics of Resistive Switching Pt/SrTiO₃ Junctions. *J. Korean Phys. Soc.* **57**, 1432–1436 (2010).
- 50. Wang, Q. & He, D. Time-decay Memristive Behavior and diffusive dynamics in one forget process operated by a 3D vertical Pt/Ta₂O₅-x/W device. *Sci. Rep.* **7**, 1–8 (2017).
- 51. Heisig, T. *et al.* Oxygen Exchange Processes between Oxide Memristive Devices and Water Molecules. *Adv. Mater.* **30**, 1–7 (2018).
- 52. Baeumer, C. *et al.* Spectromicroscopic insights for rational design of redox-based memristive devices. *Nat. Commun.* **6**, (2015).
- 53. Hensling, F. V. E., Heisig, T., Raab, N., Baeumer, C. & Dittmann, R. Tailoring the switching performance of resistive switching SrTiO₃ devices by SrO interface engineering. *Solid State Ionics* **325**, 247–250 (2018).
- 54. Gao, S. *et al.* An Oxide Schottky Junction Artificial Optoelectronic Synapse. *ACS Nano* (2019) doi:10.1021/acsnano.9b00340.
- 55. Tarun, M. C., Selim, F. A. & McCluskey, M. D. Persistent photoconductivity in strontium titanate. *Phys. Rev. Lett.* (2013) doi:10.1103/PhysRevLett.111.187403.
- 56. Poole, V. M., Huso, J. & McCluskey, M. D. The role of hydrogen and oxygen in the persistent photoconductivity of strontium titanate. *J. Appl. Phys.* **123**, (2018).
- 57. Hensling, F. V. E. *et al.* UV radiation enhanced oxygen vacancy formation caused by the PLD plasma plume. *Sci. Rep.* **8**, 4–10 (2018).
- 58. Suwanwong, S. *et al.* The dynamics of ultraviolet-induced oxygen vacancy at the surface of insulating SrTiO₃ (0 0 1). *Appl. Surf. Sci.* **355**, 210–212 (2015).
- 59. Wang, Y. *et al.* UV-induced desorption of oxygen at the TiO₂ surface for highly sensitive room temperature O₂ sensing. *J. Alloys Compd.* **793**, 583–589 (2019).
- 60. Morgan, B. J. & Watson, G. W. A density functional theory + u study of Oxygen vacancy formation at the (110), (100), (101), and (001) surfaces of rutile TiO₂. *J. Phys. Chem. C* **113**, 7322–7328 (2009).
- 61. Janotti, A., Varley, J. B., Choi, M. & Van De Walle, C. G. Vacancies and small polarons in SrTiO₃. *Phys. Rev. B - Condens. Matter Mater. Phys.* **90**, 1–6 (2014).

62. Quach, V. D. *et al.* Oxygen Vacancy Formation at Metal–TiO₂ Interface Yielding Enhanced Photocatalytic Hydrogen Generation. *Adv. Sci.* **01835**, (2025).
63. Tamura, T., Ishibashi, S., Terakura, K. & Weng, H. First-principles study of the rectifying properties of Pt/ TiO₂ interface. *Phys. Rev. B - Condens. Matter Mater. Phys.* **80**, 1–6 (2009).
64. Zhang, Z. & Janotti, A. Cause of extremely long-lasting room-temperature persistent photoconductivity in SrTiO₃ and related materials. *Phys. Rev. Lett.* **125**, 126404 (2020).
65. Gao, T. *et al.* Giant Switchable Persistent Photoconductivity in Soft Chemistry Reduced SrTiO₃. *Adv. Electron. Mater.* **9**, 3–9 (2023).
66. Saadatkia, P., Stepanov, P. & Selim, F. A. Photoconductivity of bulk SrTiO₃ single crystals at room temperature. *Mater. Res. Express* **5**, (2018).
67. Kim, H., Mahmoodi, M., Nili, H. & Strukov, D. B. 4K-memristor analog-grade passive crossbar circuit. *Nat. Commun.* **12**, 5198 (2021).
68. Mikaitis, M., Pineda García, G., Knight, J. C. & Furber, S. B. Neuromodulated Synaptic Plasticity on the SpiNNaker Neuromorphic System. *Front. Neurosci.* **12**, 1–13 (2018).
69. Pfeiffer, M. & Pfeil, T. Deep Learning With Spiking Neurons: Opportunities and Challenges. *Front. Neurosci.* **12**, (2018).
70. Rodriguez, H. G., Guo, Q. & Moraitis, T. Short-Term Plasticity Neurons Learning to Learn and Forget. (2022).
71. Orvieto, A. *et al.* Resurrecting Recurrent Neural Networks for Long Sequences. *Proc. Mach. Learn. Res.* **202**, 26670–26698 (2023).
72. Chang, T., Jo, S.-H. & Lu, W. Short-term memory to long-term memory transition in a nanoscale memristor. *ACS Nano* **5**, 7669–7676 (2011).
73. Giotis, C. *et al.* Bidirectional volatile signatures of metal–oxide memristors—Part I: Characterization. *IEEE Trans. Electron Devices* **67**, 5158–5165 (2020).
74. Nie, F. *et al.* Ultrathin SrTiO₃-based oxide memristor with both drift and diffusive dynamics as versatile synaptic emulators for neuromorphic computing. *Mater. Futur.* **2**, 35302 (2023).
75. Li, H., Geng, S., Liu, T., Cao, M. & Su, J. Synaptic and gradual conductance switching behaviors in CeO₂/Nb–SrTiO₃ heterojunction memristors for electrocardiogram signal recognition. *ACS Appl. Mater. Interfaces* **15**, 5456–5465 (2023).
76. Mikheev, E., Hoskins, B. D., Strukov, D. B. & Stemmer, S. Resistive switching and its suppression in Pt/Nb:SrTiO₃ junctions. *Nat. Commun.* **5**, (2014).
77. Du, C., Ma, W., Chang, T., Sheridan, P. & Lu, W. D. Biorealistic Implementation of Synaptic Functions with Oxide Memristors through Internal Ionic Dynamics. *Adv. Funct. Mater.* **25**, 4290–4299 (2015).

Supplementary

S1 Calculation of energy per optical pulse

The energy per optical pulse per device is given by the following equation:

$$E_{pulse} = P_{pulse} \cdot A_{device} \cdot w_{pulse}$$

with P_{pulse} being the power density of the optical signal, A_{device} the device pitch area and w_{pulse} the width of the pulse. For our values ($P_{pulse} = 65 \text{ mWcm}^{-2}$, $w_{pulse} = 1 \text{ ms}$) and an assumed device pitch area of $A_{device} = 0.5625 \mu\text{m}^2$ a pulse energy of 0.3655 pJ is calculated.

S2 Fitting Model

The fitting parameters for the SET decay model and the optical decay model are given in Table S1 and Table S2 respectively for the three applied bias voltages.

Parameter	Bias Voltage	Value
G_{steady}	0.6V	9.3 nS
	0 V	3.0 nS
	-0.6 V	0.4 nS
$\Delta G^{(SET)}$	0.6V	37.6 nS
	0 V	34.0 nS
	-0.6 V	10.1 nS
$\gamma^{(SET)}$	0.6V	0.7989
	0 V	0.8629
	-0.6 V	0.7872
$\tau_1^{(SET)}$	0.6V	5.4 s
	0 V	1.1 s
	-0.6 V	0.8 s
$\tau_2^{(SET)}$	0.6V	218.7 s
	0 V	7.5 s
	-0.6 V	2.2 s
β	0.6V	0.19
	0 V	0.27
	-0.6 V	0.26
$\langle \tau_2^{(SET)} \rangle$	0.6V	36863 s
	0 V	99.1 s
	-0.6 V	40.9 s

Table S 1: Fitting parameters of SET decay model

Parameter	Bias Voltage	Value
G_{steady}	0.6V	9.7 nS
	0 V	3.2 nS
	-0.6 V	0.5 nS
$\Delta G^{(opt)}$	0.6V	4 nS
	0 V	3.4 nS
	-0.6 V	1 nS
$\gamma^{(opt)}$	0.6V	0.6704
	0 V	2.295
	-0.6 V	2.944
$\tau_1^{(opt)}$	0.6V	4.5 s
	0 V	1.6 s
	-0.6 V	1 s
$\tau_2^{(opt)}$	0.6V	44.6 s
	0 V	20.5 s
	-0.6 V	15 s

Table S 2: Fitting parameters for optical decay model

S3 Measurement protocols

Two different measurement protocols were used to obtain the conductance state dependent photoresponse in Fig. 4a. (1) The first protocol employs multiple individual 4V/1ms pulses to repeatedly SET the device to a higher conductance state as shown in Fig. S1a, whereas (2) the second protocol SETs the device once using 100, 4V/1ms pulses (Fig. S1b). The optical conductance change was extracted for several measurements for each of the two protocols, resulting in Fig. 4c. The size of the marker determines the protocol (protocol 1 = small markers, protocol 2 = big markers) and the color stands for the timing of the optical pulse relative to the SET pulse.

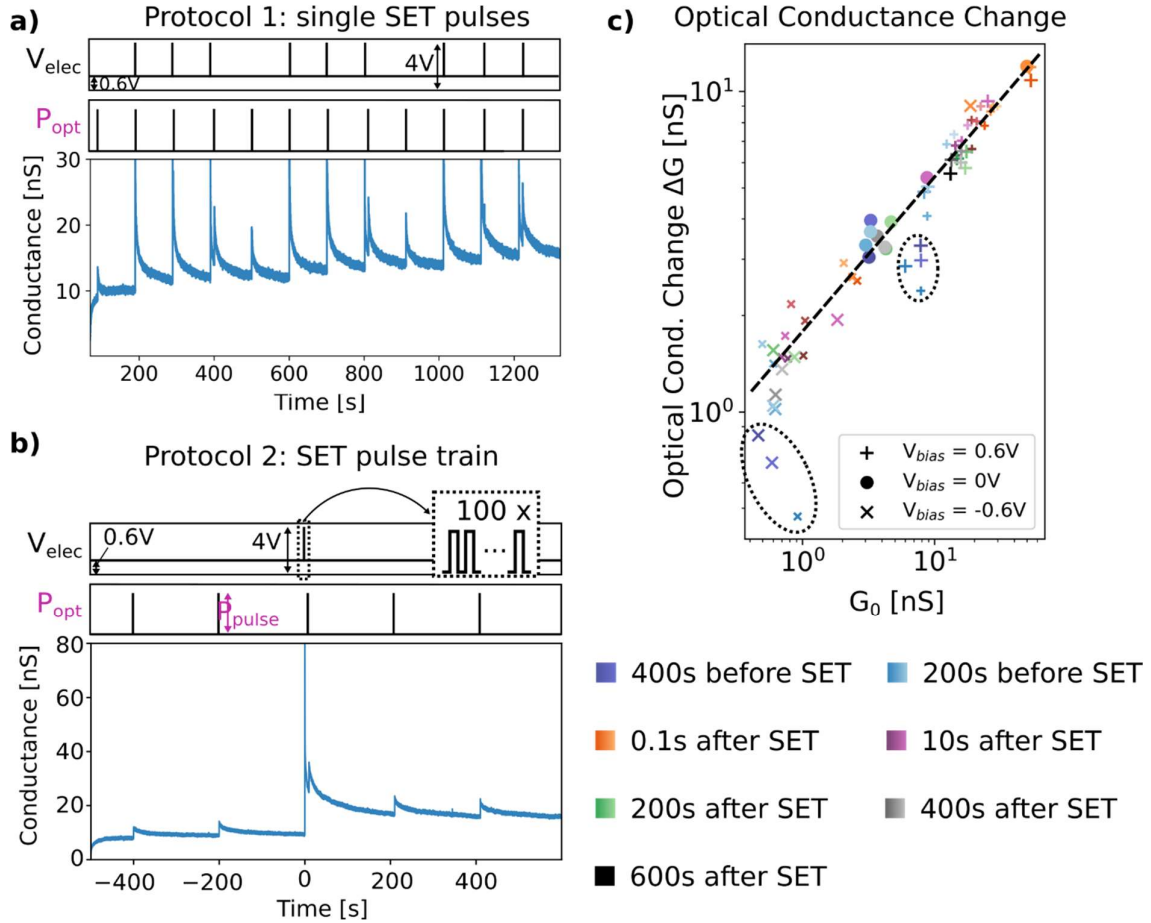


Figure S1: a) Measurement protocol 1, where the device is SET using individual SET pulses. b) Measurement protocol 2, where the device is SET using a pulse train of 100 pulses. c) The conductance state dependent photoresponse extracted from the two measurement protocols as a function of the initial conductance state.

S4 Measurements with subtracted initial conductance state

To compare the optical decay before and after SET the fitted electrical conductance state $G_0(t)$ was subtracted from the data in Fig. S2. The effect of the bias voltage V_{bias} on the optical decay without the electrical decay component is visible: The larger V_{bias} the slower the decay.

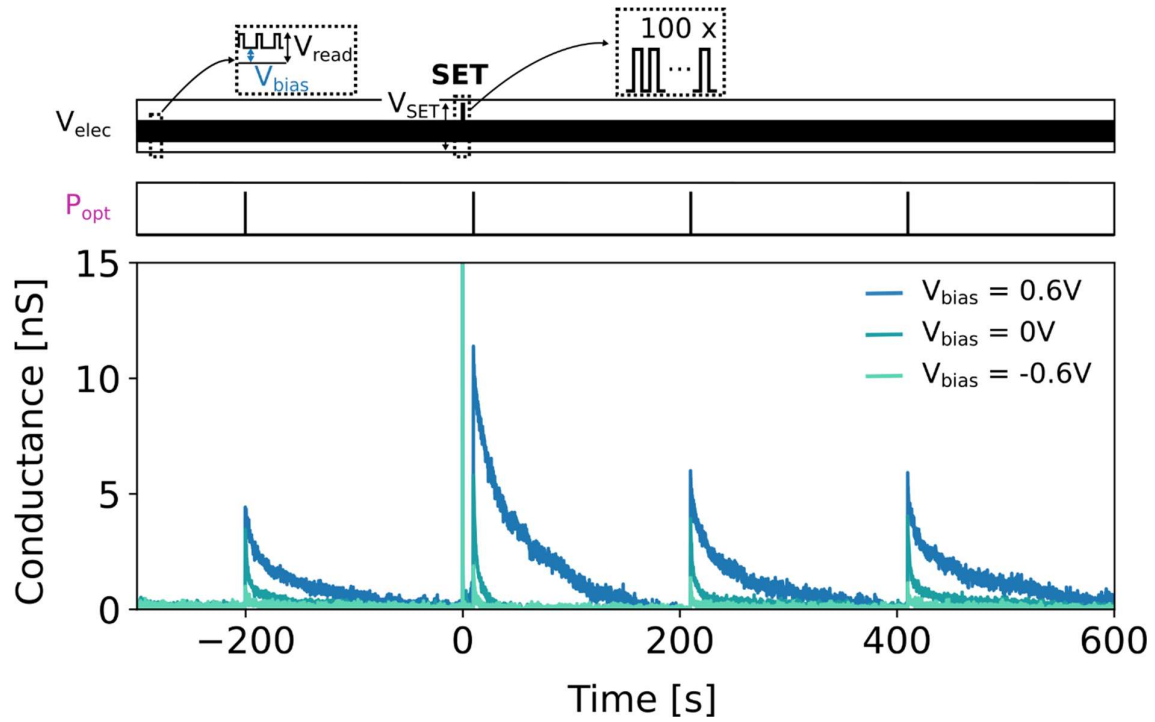


Figure S2: Measurement of Fig 3a in the range of [-300 s, 600 s] with the electrical conductance state $G_0(t)$ subtracted from the data.